Pressure-driven transport of particles through a converging-diverging microchannel

Ye Ai,[1] Sang W. Joo,[2] Yingtao Jiang,[3] Xiangchun Xuan,[4] and Shizhi Qian[1,a)]
[1]*Department of Aerospace Engineering, Old Dominion University, Norfolk, Virginia 23529, USA*
[2]*School of Mechanical Engineering, Yeungnam University, Gyongsan 712749, South Korea*
[3]*Department of Electrical and Computer Engineering, University of Nevada Las Vegas, Las Vegas, Nevada 89154, USA*
[4]*Department of Mechanical Engineering, Clemson University, Clemson, South Carolina 29634, USA*

(Received 13 January 2009; accepted 30 March 2009; published online 22 April 2009)

Pressure-driven transport of particles through a symmetric converging-diverging microchannel is studied by solving a coupled nonlinear system, which is composed of the Navier–Stokes and continuity equations using the arbitrary Lagrangian–Eulerian finite-element technique. The predicted particle translation is in good agreement with existing experimental observations. The effects of pressure gradient, particle size, channel geometry, and a particle's initial location on the particle transport are investigated. The pressure gradient has no effect on the ratio of the translational velocity of particles through a converging-diverging channel to that in the upstream straight channel. Particles are generally accelerated in the converging region and then decelerated in the diverging region, with the maximum translational velocity at the throat. For particles with diameters close to the width of the channel throat, the usual acceleration process is divided into three stages: Acceleration, deceleration, and reacceleration instead of a monotonic acceleration. Moreover, the maximum translational velocity occurs at the end of the first acceleration stage rather than at the throat. Along the centerline of the microchannel, particles do not rotate, and the closer a particle is located near the channel wall, the higher is its rotational velocity. Analysis of the transport of two particles demonstrates the feasibility of using a converging-diverging microchannel for passive (biological and synthetic) particle separation and ordering. © *2009 American Institute of Physics.* [DOI: 10.1063/1.3122594]

I. INTRODUCTION

Transport of particles, including biological entities such as DNAs and proteins, through a microchannel or nanotube has been of significant interest with the recent development of lab-on-a-chip devices for biomedical and environmental applications.[1–4] Pressure-driven flows in particular have been widely used in various lab-on-a-chip devices.[5–7] A variety of micropumps, actuating pressure-driven flows, have been fabricated and successfully integrated into these devices.[8,9] Extensive experimental and theoretical studies have been performed on the particle transport subjected to pressure-driven flows. Cylindrical channels[10–14] have been frequently considered, as discussed in a recent comprehensive review by Al Quddus *et al.*[15] Rectangular ducts have been studied, for example, by Staben and co-workers.[16,17]

Recently, microchannels and nanotubes with nonuniform cross sections have attracted considerable attention due to their unique potential in both biological and synthetic particle transport

a)Author to whom correspondence should be addressed. Electronic mail: sqian@odu.edu.

enhancement. In particular, converging-diverging microchannels have been successfully utilized to achieve microsecond electrophoresis[18] and to sort particles using electrophoresis[19,20] and separate cells using dc dielectrophoresis.[21] With combined electro-osmotic and pressure-driven flows, particles can be concentrated, manipulated, and captured in a converging-diverging microchannel.[22] Subjected to pure pressure-driven flows, particles experience acceleration and then deceleration through the converging-diverging microchannels, which has been experimentally visualized and suggested for particle separation.[23] In addition, converging-diverging microchannels have been used to stretch deformable biological entities such as individual DNA molecules, which have important applications in genomic analysis.[24–26]

Theoretical predictions on particle dynamics driven by the pressure gradient through a converging-diverging channel have not yet been reported with precision due to the compounded difficulties with fluid-particle interactions and nonuniform geometry. For simulations of fluid-solid systems, the interactive effect on both the fluid flow and the solid deformation or movement should be taken into account simultaneously for accurate prediction. The arbitrary Lagrangian–Eulerian (ALE) algorithm has been considered as one of the most effective approaches for the simulations of fluid-solid interactions and is widely used to predict particle motions in both Newtonian and viscoelastic fluids[27,28] and electrophoresis through various microchannels[29–34] with an experimental verification.[35] The ALE method was recently employed to predict the pressure-driven transport of a spherical particle through a straight cylindrical channel, which was verified by comparing the calculated wall correction factor to analytical solutions.[15] Transient simulation of the pressure-driven transport of particles through a microchannel with varying cross-sectional areas, such as the converging-diverging microchannel, is not completed previously and is taken to be the subject of the present study.

In the ensuing sections, mathematical models for the fluid motion, particle transport, and ALE kinematics are described first. Numerical methodology and code validation then are described. Subsequently, the effects of the applied pressure gradient, particle size, geometry of the converging-diverging microchannel, and initial transverse location of the particle on its transport are investigated. Particle separation is also demonstrated and analyzed. The results will quantitatively show translational and rotational enhancements of particles moving through converging-diverging microchannels, which manifest potential applications to particle separation, orderly particle transport, and stretching of deformable biological entities in lab-on-a-chip devices.

II. MATHEMATICAL MODEL

Figure 1(a) shows a two-dimensional (2D) model of a circular particle transport in a converging-diverging microchannel, which is based on the fabricated device used in the experiments of Xuan and Li,[23] shown in Fig. 1(b). The computational domain Ω is surrounded by the boundary ABCDEFGHIJ and Γ. The segments AJ and EF are the inlet and the outlet, respectively, between which a pressure difference is applied. The segments ABCDE and FGHIJ are the channel walls. Γ is the particle surface, which is initially located in the upstream straight section. The width of the straight section and the throat are, respectively, a and b. The particle diameter and the vertical distance between the particle center and the channel axis are d and h, respectively. L_a, L_b, L_c, and L_d denote the length of upstream straight, converging, diverging, and downstream straight sections, respectively. The upstream straight section is long enough for particles to gain a fully developed motion before they enter into the converging section. The particle and channel walls are rigid, and the fluid in the computational domain Ω is incompressible and Newtonian. The effects of Brownian motion and gravity are ignored.

The conservations of fluid mass and momentum are described by the continuity equation and the Navier–Stokes (NS) equations,

$$\nabla \cdot \mathbf{u} = 0 \quad \text{in } \Omega \tag{1}$$

and

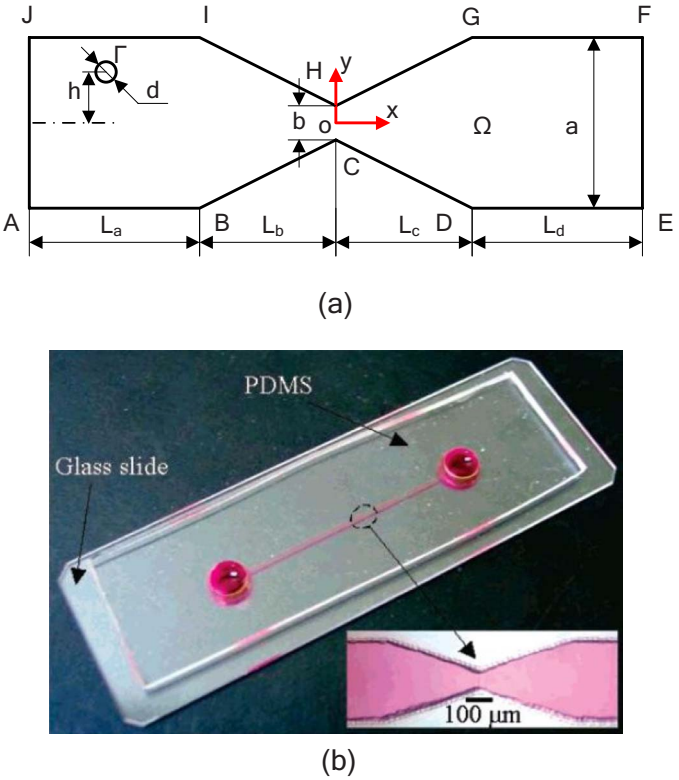

FIG. 1. (a) Schematic view of a 2D model of a circular particle in a converging-diverging microchannel. The narrowest part is defined as the throat of the converging-diverging microchannel. The origin of the coordinate system is fixed at the center of the throat. (b) Photograph of a fabricated converging-diverging microchannel on a polydimethylsiloxane device. The inset is a magnified view of the converging-diverging microchannel under a microscope.

$$\rho\left(\frac{\partial \mathbf{u}}{\partial t} + \mathbf{u}\cdot\nabla\mathbf{u}\right) = -\nabla p + \eta\nabla^2\mathbf{u} \quad \text{in } \Omega, \tag{2}$$

where $\mathbf{u}$ is the velocity vector, p is the pressure, ρ and η are the density and viscosity of the fluid, respectively, and t is the time.

A pressure difference ΔP is imposed between the inlet AJ and the outlet EF. The effect of streaming potential field on the particle transport is generally low,[23] and so the electrophoretic motion of the suspended particle is ignored. The no-slip condition is applied on the channel walls ABCDE and FGHIJ. Since the particle translates and rotates simultaneously, the boundary condition for the fluid on the particle surface contains both translational velocity and rotational velocity,

$$\mathbf{u} = \mathbf{U_p} + \boldsymbol{\omega_p}\times(\mathbf{x_s} - \mathbf{x_p}) \quad \text{on } \Gamma, \tag{3}$$

where $\mathbf{U_p}$, $\boldsymbol{\omega_p}$, $\mathbf{x_s}$, and $\mathbf{x_p}$ are the translational velocity, the rotational velocity, the position vector of the particle surface, and the position vector of the particle center, respectively.

The translational velocity of the particle is determined by Newton's second law

$$m_p\frac{d\mathbf{U_p}}{dt} = \mathbf{F}, \tag{4}$$

where m_p is the mass of the particle and $\mathbf{F}$ is the net force exerted on the particle due to the external flow field surrounding it, which can be expressed as

$$\mathbf{F} = \int (\boldsymbol{\sigma} \cdot \mathbf{n}) d\Gamma. \tag{5}$$

Here $\mathbf{n}$ is the unit outward normal vector and $\boldsymbol{\sigma}$ is the hydrodynamic stress tensor

$$\boldsymbol{\sigma} = -p\mathbf{I} + \eta(\nabla \mathbf{u} + \nabla \mathbf{u}^T), \tag{6}$$

where $\mathbf{I}$ is the identity tensor.

The rotational velocity of the particle is governed by

$$\boldsymbol{I}_p \frac{d\omega_p}{dt} = \mathbf{T} = \int (\mathbf{x_s} - \mathbf{x}_p) \times (\boldsymbol{\sigma} \cdot \mathbf{n}) d\Gamma, \tag{7}$$

where $\boldsymbol{I}_p$ is the moment of inertial of the particle and $\mathbf{T}$ is the torque exerted on the particle by the flow field.

The center $\mathbf{x_p}$ and orientation θ_p of the particle are governed by the dynamic equations

$$\mathbf{x_p} = \mathbf{x_{p0}} + \int_0^t \mathbf{U_p} dt \tag{8}$$

and

$$\theta_p = \theta_{p0} + \int_0^t \omega_p dt, \tag{9}$$

where $\mathbf{x_{p0}}$ and θ_{p0} denote the initial location and orientation of the particle, respectively.

III. COMPUTATIONAL METHOD AND CODE VALIDATION

For simulations of particle transport in a channel, the ALE finite-element method is used to solve the fluid flow field in the Eulerian reference frame, and meanwhile track the particle motion in a Lagrangian fashion. Here, the Eulerian reference frame and the Lagrangian reference frame are fixed to the spatial space and the computational mesh, respectively. The computational domain Ω in Fig. 1(a) is discretized into quadratic triangular elements with a higher concentration of elements around the particle surface and the throat. Due to the implementation of the ALE kinematics, the NS equation (2) is modified as

$$\rho\left(\frac{\partial \mathbf{u}}{\partial t} + (\mathbf{u} - \mathbf{u_m}) \cdot \nabla \mathbf{u}\right) = -\nabla p + \eta \nabla^2 \mathbf{u} \quad \text{in } \Omega. \tag{10}$$

In the above, $\mathbf{u_m}$ is the mesh velocity relative to the Eulerian reference frame, which satisfies a Laplace equation to guarantee its smooth variation,[28]

$$\nabla \cdot (k^e \nabla \mathbf{u_m}) = 0, \tag{11}$$

where k^e is a function to control the deformation of the domain such that the region away from the particles absorbs most of the deformation, while the region next to the particles is relatively stiff and retains its shape better. We choose k^e to be the inverse of the local element volume. The boundary conditions for the mesh velocity satisfy $\mathbf{u_m} = \mathbf{U_p} + \boldsymbol{\omega_p} \times (\mathbf{x_s} - \mathbf{x_p})$ on the particle surface and the fixed boundary condition on the wall, inlet, and outlet of the microchannel.

An explicit-implicit scheme, adopted by Hu *et al.*,[28] is used to solve the fluid-particle system. Briefly, after each computational time step, the particle location and the mesh in the fluid domain are updated explicitly and followed by a mesh quality check. When the mesh quality degrades to a designated level as the particle translates and rotates, the deformed mesh is used to create a new geometry upon which a new mesh is generated to continue the computation until the next mesh degradation. Figures 2(a) and 2(b) depict the undeformed mesh and deformed mesh adjacent to the

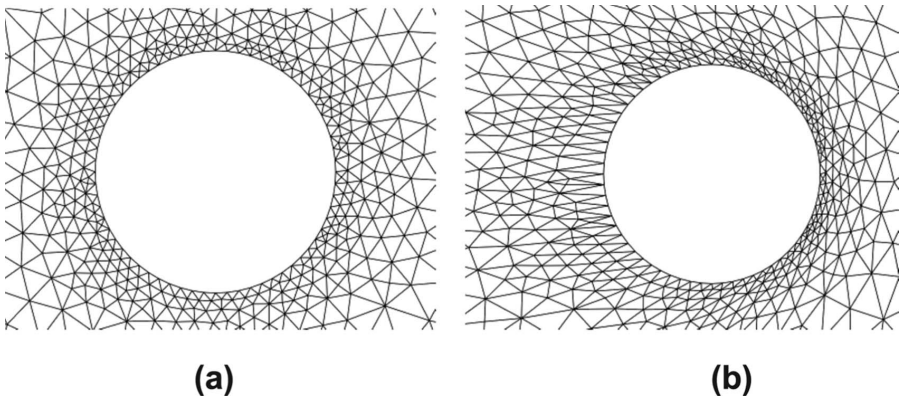

FIG. 2. Undeformed (a) and deformed (b) mesh adjacent to the particle surface.

particle surface, respectively. After that, the solution of the fluid flow field from the old mesh is mapped onto the new mesh. Finally, the particle's translational and rotational velocities, the fluid flow field, and the mesh velocity are solved implicitly. The explicit-implicit scheme is second-order accurate in time and is numerically stable.

The aforementioned ALE finite-element method for direct numerical simulation of the fluid-particle system is implemented with the use of a high-level programming-language based on the commercial finite-element package COMSOL (Version 3.4a, www.comsol.com), which is extremely versatile for solving systems of coupled partial differential equations, installed in a 64-bit dual-processor workstation with 64 Gbyte RAM. Since the moving boundary due to the particle's motion is not predefined in COMSOL's application modes, the fluid-particle system could not be directly solved under COMSOL's graphical user interface . We have chosen to use the scripting capabilities of COMSOL in combination with MATLAB and implemented the aforementioned ALE algorithm manually in MATLAB. The use of the COMSOL reduces the programming effort to a minimum. Numerical solutions presented in this study are fully converged, with an absolute error bound of 10^{-6} and minimum element number of 5200 with 64 on the particle surface, through rigorous mesh-refinement tests.

The developed ALE code has been validated by several benchmark test problems. We first reproduce the wall correction factor of a spherical particle translating along the axis of a cylindrical channel using a 2D axisymmetric model. The wall correction factor G, which presents the lag effect of the channel wall on the particle transport, is defined as the ratio of the particle's steady translational velocity to the maximum flow velocity along the axis. Figure 3 shows the relationship between the wall correction factor G and the ratio of the particle diameter to the channel diameter, d/a. The wall correction factor predicted by the present NS-ALE model agrees well with the analytical solutions[11,13] and existing numerical results.[15] The analytical solution obtained by Haberman and Sayre is valid only when the ratio d/a is smaller than 0.8 since only ten terms in the Fourier series of the Stokes stream function were used in their derivation.[11] Its prediction thus deviates from our numerical modeling for $d/a > 0.8$, as demonstrated in Fig. 3. We then simulated particle transport in a converging-diverging microchannel driven by a pressure-driven flow, and our computational results are in good agreement with the existing experimental data (Fig. 5 in Sec. IV). In addition, the same ALE algorithm has been successfully exploited to investigate transient electrophoretic motions of particles in microchannels with spatially nonuniform electric fields, and the predictions are also in good agreement with the existing experimental data.[36]

IV. RESULTS AND DISCUSSION

With the reliability of the present method and implementation fully established, we study the particle motion in a converging-diverging channel. The dimensions of the microchannel are taken

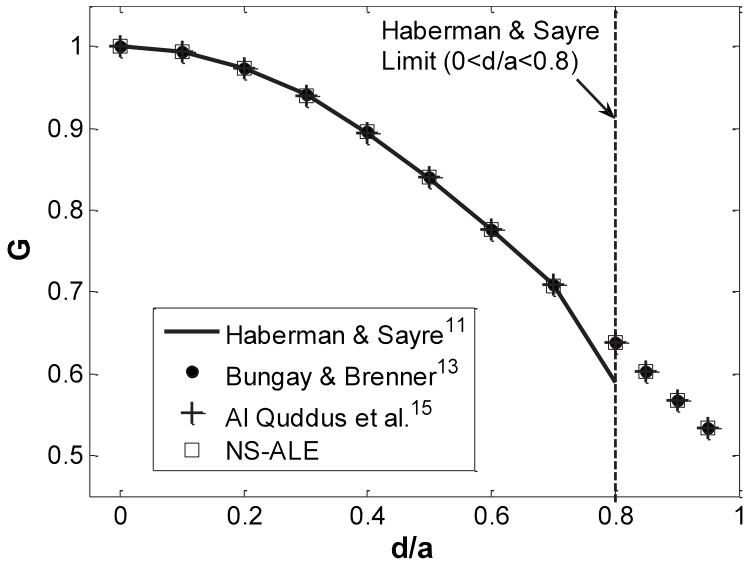

FIG. 3. Wall correction factor G of a spherical particle moving along the axis of a cylindrical infinite channel. The dashed line indicates the limit of Haberman and Sayre's analytical solution (Ref. 11).

from the channel in Xuan and Li's experiments,[23] which is symmetric about the channel throat with $L_b=L_c=400$ μm. The total length L of the microchannel in our model is taken to be 1500 μm with $L_a=400$ and $L_d=300$ μm, which is shorter than the real channel length L' while still capturing the main features. In order to impose the same pressure gradient as in the experiment, the pressure difference applied between the inlet and the outlet is assigned by scaling that in the experiment ΔP with the ratio L/L'. For convenience in the comparisons of present computational results and the experimental data, the pressure difference applied in the model is labeled by the actual pressure difference applied in the experiment. As the exact pressure gradient (produced by manually adjusting the liquid height difference in the upstream and downstream wells) in the experiment of Xuan and Li was unknown, we estimate the applied pressure difference ΔP in our model to match the particle speed in the experiment, and the predicted results for other pressure differences (i.e., $2\Delta P/3$ and $\Delta P/3$) agree well with the corresponding experimental results. The Reynolds number of the fluid flow in the upstream straight channel corresponding to ΔP is about 0.22. The fluid in the computational domain Ω is pure water, as in the experiment. The width a in the straight sections is 325 μm, and the throat width b is set to 55 μm except for the parametric study on the throat width.

A. Transient transport of a particle

The sequential images in Fig. 4(a) illustrate the movement of a particle ($d=20$ μm) along the centerline of the converging-diverging microchannel based on the present NS-ALE model, which appears to be in good qualitative agreement with those observed in the experiment, as shown in Fig. 4(b). The pressure differences applied in simulation and in experiment are both $2\Delta P/3$. The time intervals between images in Figs. 4(a) and 4(b) are 0.2 s.

B. Effect of pressure gradient

Three different pressure differences (ΔP, $2\Delta P/3$, and $\Delta P/3$) were applied to drive a 20 μm particle moving along the centerline of the converging-diverging microchannel in the experiments of Xuan and Li. Using the same pressure gradients, simulations are performed to study the effect of the pressure gradient on the particle transport. Figure 5(a) shows the translational velocity of a 20 μm particle moving along the centerline of the converging-diverging microchannel under the three pressure gradients. The numerical results (lines) agree well with the corresponding experi-

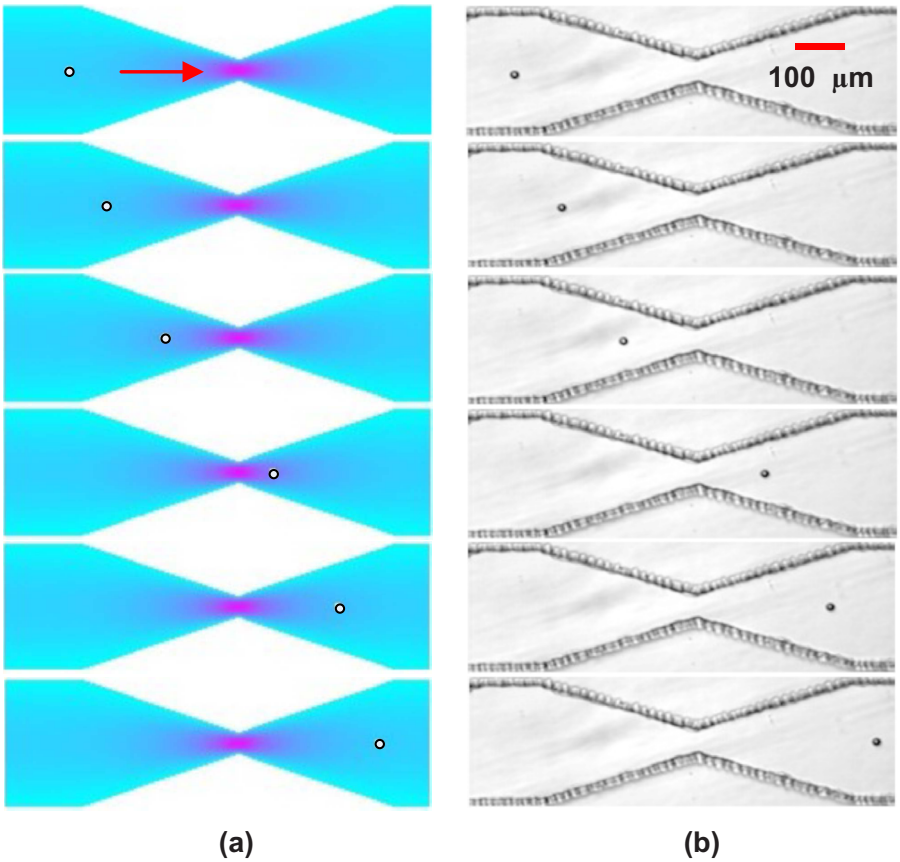

FIG. 4. Sequential images of a particle of 20 μm in diameter moving along the centerline of the converging-diverging microchannel under a pressure difference of $2\Delta P/3$. The arrow denotes the direction of the particle transport. The time interval between adjacent images is 0.2 s. (a) The particle trajectory predicted by the NS-ALE model. The particle is marked with a circle. The color levels denote the magnitude of the fluid velocity with the maximum fluid velocity at the throat. (b) Experimental images captured by an inverted microscope with a charge-coupled device camera.

mental data (symbols). The small discrepancies can be attributed to the reading error of the experimental data and to the dimensional simplification in computations. Error bars of ± 50 μm/s are added to the experimental data for $2\Delta P/3$ for comparison.

In all cases the particle experiences monotonic acceleration, followed by deceleration with symmetry about the throat. The higher the applied pressure difference is, the higher is the translational velocity. Relying on the gradual enhancement in the particle's translational velocity through a converging channel, deformable biological entities such as individual DNA molecules can be stretched.[24,25]

Figure 5(b) shows the ratio λ of the translational velocity to that in the upstream straight section under the three different pressure gradients. Due to the reading error of ± 50 μm/s in the experiment, the translational velocity ratio under the pressure difference of $2\Delta P/3$ shows an error of $\pm 10\%$. The computational results (lines) fall between the error bars and are in good agreement with the experiment data (symbols). Further studies on the ratio of the translational velocity at the throat to that in the upstream straight channel δ, under a large range of pressure difference from $\Delta P/3$ to $10\Delta P$, suggest that the translational velocity ratio is independent of the applied pressure gradient. This also confirms that the wall correction factor does not vary with the pressure gradient. The translational velocity ratio at the throat is approximately 4.83, which is lower than 5.91, the cross-sectional area ratio of the straight section to the throat. It should be attributed to the lag effect of the channel wall.

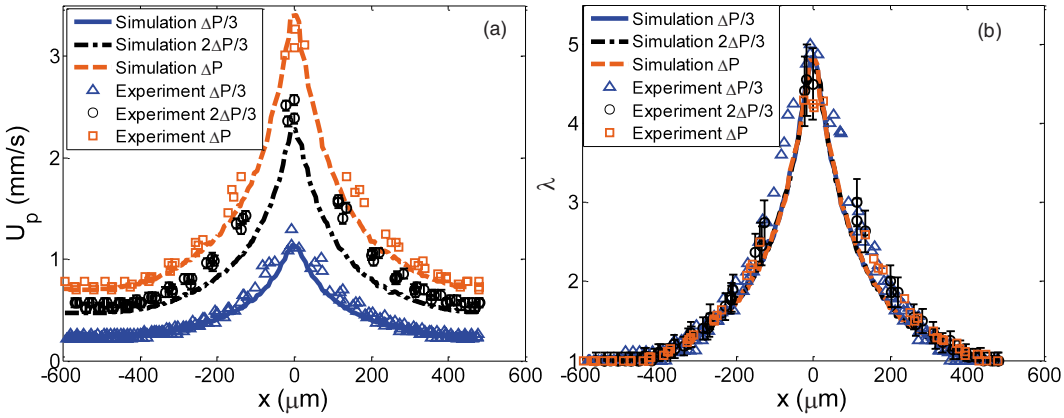

FIG. 5. Translational velocity profiles (a) and velocity ratios (b) of a particle of 20 μm in diameter moving along the centerline of the converging-diverging microchannel under different pressure differences. The x axis denotes the centerline of the microchannel, and the zero x coordinator represents the throat of the converging-diverging microchannel. Lines denote the numerical results and symbols represent the existing experimental data.

C. Effect of particle size

Figure 6 shows the translational velocity ratio of particles with different diameters moving along the centerline of the converging-diverging microchannel under the pressure difference ΔP. The particle size has a significant impact on its motion. Smaller particles result in higher translational velocity ratios at the throat. With diameters of less than 48 μm, particles accelerate monotonically toward the throat. Particles with diameter closer to the throat size of 55 μm experience more complicated acceleration-deceleration stages. The 48 μm particle, for example, accelerates in the converging section (from point A to point B). When it is 46 μm away from the throat (point

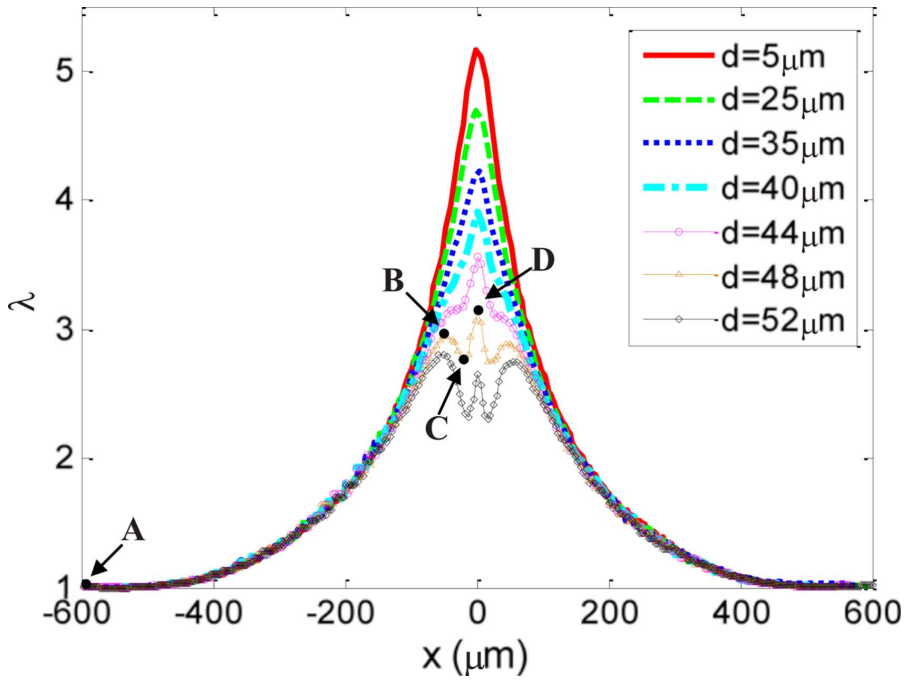

FIG. 6. Translational velocity ratios of particles with different sizes moving along the centerline of the converging-diverging microchannel under a pressure difference of ΔP. The throat width is b=55 μm. The x coordinators of points A, B, C, and D are −600 μm, −46 μm, −20 μm, and 0, respectively.

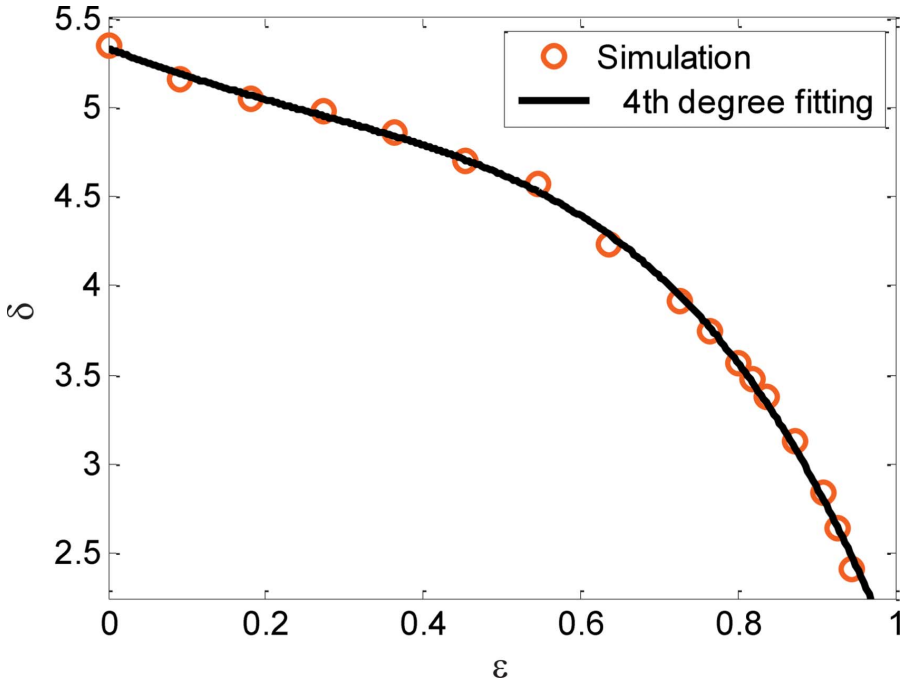

FIG. 7. The relationship between the ratio of the particle size to the throat width and the translational velocity ratio at the throat under a pressure difference of ΔP. The throat width is $b=55$ μm. The circles and solid line denote the numerical results and the fourth degree polynomial fitting curve, respectively. The translational velocity ratio at the throat with a zero particle size refers to the ratio of the fluid velocity at the throat to that in the upstream straight channel.

B), it begins to decelerate (from point B to point C) until it is 20 μm away from the throat. It then reaccelerates (from point C to the throat D) with a maximum translational velocity ratio. The deceleration in the diverging section is symmetrical to the three stages in the converging section. For even larger particles, the maximum translational velocity ratio does not coincide with the throat. The 52 μm particle exhibits maximum translational velocity ratio at the end of the first acceleration stage.

Figure 7 depicts the relation between the ratio of the particle diameter to the throat width ε and the translational velocity ratio δ at the throat. The maximum δ occurs in the absence of any particle being transported. As ε increases from zero, δ decreases, which is similar to the trend of the wall correction factor G shown in Fig. 3. The solid line in Fig. 7 represents the fourth degree polynomial fitting of the numerical results

$$\delta = -2.9335\varepsilon^4 - 0.12106\varepsilon^3 + 1.3152\varepsilon^2 - 1.6731\varepsilon + 5.3305. \quad (12)$$

The above equation can be used to evaluate the translational velocity ratio at the throat unless the particle diameter is very close to the throat width.

D. Effect of the cross-sectional area

The ratio of the cross-sectional area of the throat to that of the upstream straight section ξ characterizes the contraction and expansion structure of the microchannel, which must be optimized in real applications to obtain a desired translational velocity ratio at the throat. Figure 8 shows the relationship between ξ and the translational velocity ratio δ at the throat for two different particle sizes. As the throat size approaches the width of the straight section, the translational velocity ratio at the throat δ becomes unity, as expected. The solid line, referring to the absence of a particle, is shown to be the upper limit for δ. As the particle size decreases, the solid line will be approached. A small value of ξ significantly increases the wall lag effect at the throat.

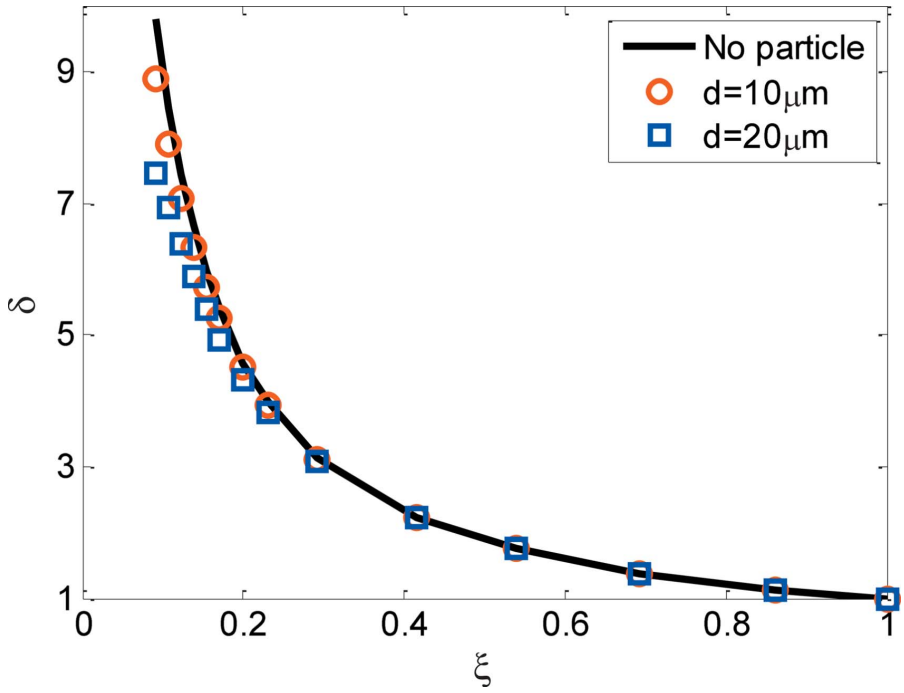

FIG. 8. Effect of the cross-sectional area ratio between the throat and the straight channel on the translational velocity ratio at the throat with two different particle sizes. The pressure difference applied between the inlet and the outlet is ΔP. The width of the straight microchannel is 325 μm. The solid line indicates the ratio of the fluid velocity at the throat to that in the upstream straight channel without particle transport through it.

As a result, the discrepancies between the solid line and the symbols increase with the decrease in the cross-sectional area ratio ξ. When ξ is 0.0923, δ for particle sizes of 10 μm and 20 μm are 75.9% and 90.6%, respectively, of that of the solid line.

E. Effect of transverse location of the particle

In this section, the effect of the initial transverse location of the particle is studied. The initial transverse location is defined by the distance h from the center of the particle to that of the microchannel. The half width of the straight channel is used to normalize the initial transverse location, thus the dimensionless distance h^* is $2h/a$.

Due to the low Reynolds number, the pressure-driven flow in the converging-diverging microchannel is laminar. Trajectories of the particles thus coincide with streamlines in the absence of particles, as observed in experiments.[23] Figure 9 displays particle trajectories computed for different initial locations, which demonstrate that the particles would move along their respective streamlines. Symmetry with respect to the throat is noted.

When a particle moves along the centerline, torque exerted on the particle is zero. However, when a particle is initially located off the centerline, the flow field around it becomes asymmetric, inducing a torque on the particle and forcing the particle to rotate. Figure 10 shows the rotational velocity of a 20 μm particle moving through the converging-diverging microchannel for two different initial locations ($h^*=0$ and $h^*=0.4$). The rotational velocity also exhibits symmetry with respect to the throat. The closer the particle initially is located near the channel wall, the higher the rotational velocity at the throat is. Moreover, the angular velocity at the throat is linearly proportional to the initial dimensionless distance h^* (the results are not shown here). It is clear that the converging-diverging microchannel can enhance the particle rotation, which must be taken into account for precise control over stretching and unfolding of deformable biological entities.

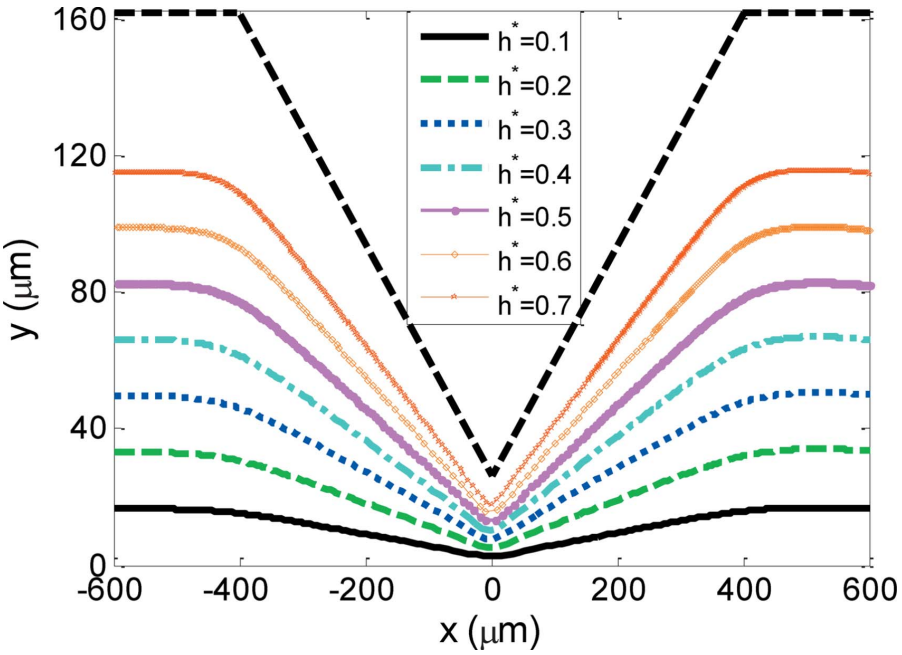

FIG. 9. Trajectories of a particle of 20 μm in diameter moving through the converging-diverging microchannel with different initial transverse locations under a pressure difference of ΔP. The black dashed bold line denotes the boundary of the converging-diverging microchannel.

F. Separation of two particles

In this section, the separation of two adjacent particles is investigated. The sequential images in Fig. 11(a) illustrate the separation of two 20 μm particles located on the centerline of the converging-diverging microchannel. The two particles move from left to right under a pressure

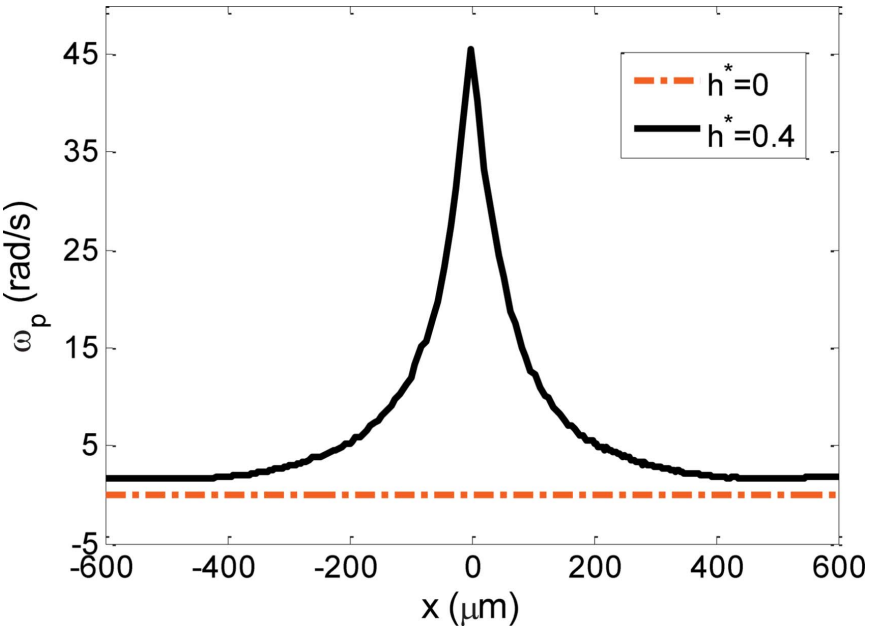

FIG. 10. Rotational velocity profiles of a particle of 20 μm in diameter moving through the converging-diverging microchannel with two different initial transverse locations under a pressure difference of ΔP.

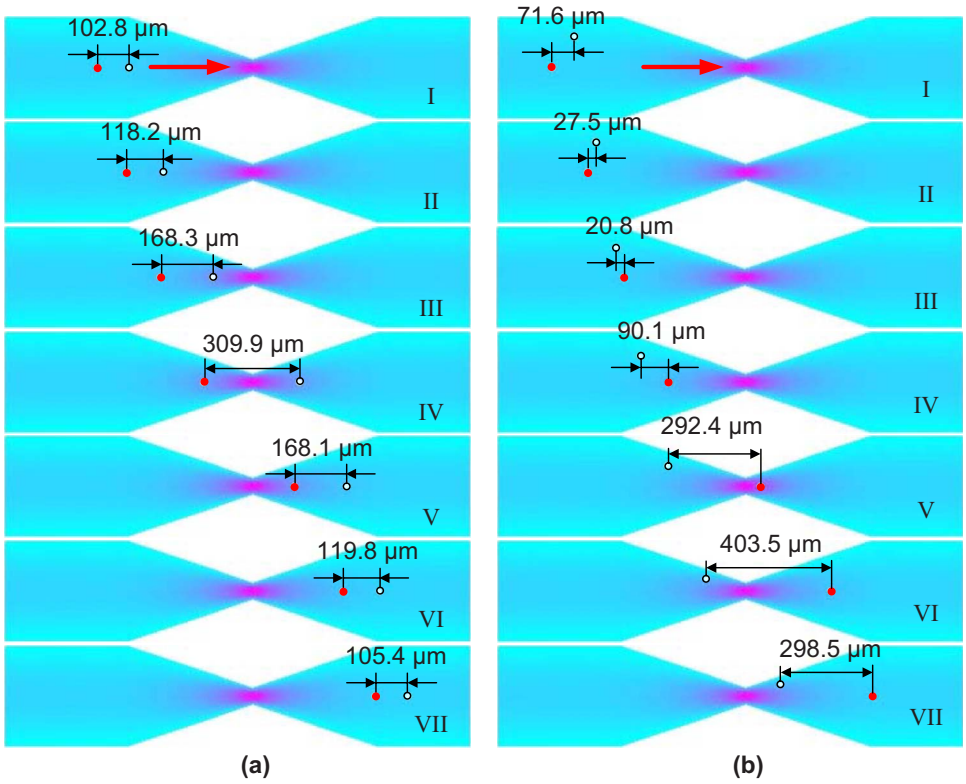

FIG. 11. Sequential images of the separation of two particles of 20 μm in diameter moving through the converging-diverging microchannel under a pressure difference of $2\Delta P/3$. The initial leading and lagging particles are, respectively, marked with a hollow circle (○) and a solid circle (●). The color levels denote the magnitude of the fluid velocity with the maximum fluid velocity at the throat. The two arrows denote the direction of particle transport. (a) Two fore-and-aft located particles moving through the microchannel. The time interval between adjacent images is 0.2 s. (b) Two up-and-down located particles moving through the microchannel. The time interval between adjacent images is 0.25 s.

difference of $2\Delta P/3$. The time interval between images is 0.2 s. The initial distance between the two identical particles is approximately 100 μm. As they pass the converging section, the distance between the two increases, as shown in Fig. 11(a) [(I)–(III)], since the leading particle (marked with a hollow circle) is accelerated sooner. The distance between the two reaches a maximum of 309.9 μm when the two particles are located symmetrically with respect to the throat, as shown in Fig. 11(a) (IV). Subsequently, the translational velocity of the lagging particle exceeds that of the leading particle, and the distance decreases, as shown in Fig. 11(a) [(V)–(VII)]. The lagging particle is gaining on the leading particle until the two particles moved out of the diverging section. Finally, it is shown that the initial distance is recovered. The separation and recovery of two particles moving along the centerline of a converging-diverging microchannel has also been observed in an electrophoresis.[19]

The separation of two 20 μm particles with different trajectories is illustrated in Fig. 11(b) with a time interval of 0.25 s. The two move from left to right under a pressure difference of $2\Delta P/3$. The leading particle (marked with a hollow circle), placed 100 μm off the centerline of the microchannel, initially is ahead of the initial lagging particle (marked with a solid circle) by approximately 70 μm. The other particle is on the centerline of the microchannel. Since the translational velocity along the centerline is larger, the distance between the two decreases gradually, as shown in Fig. 11(b) [(I) and (II)]. Subsequently, the initially lagging particle passes the initial leading particle, as shown in Fig. 11(b) (III). The distance increases further, as shown in Fig. 11(b) [(IV) and (V)], and reaches a maximum of 403.5 μm in Fig. 11(b) (VI). The particle initially behind moves out of the diverging channel, while the other enters the throat. The distance

between the two thus decreases to 298.5 μm in Fig. 11(b) (VII). The initial separation distance is not to be recovered because the two particles follow two different paths. This predicted enhancement in particle separation is consistent with the experiment.[23]

V. CONCLUSIONS

Using the transient NS-ALE finite-element model developed in this paper, we demonstrate that the converging-diverging microchannel has the ability to enhance pressure-driven transport of particles. Although higher pressure gradient leads to higher translational velocity, the ratio of the translational velocity to that in the upstream straight section is independent of the pressure gradient, and the theoretical predictions agree with the experimental observations.[23] An unusual acceleration-deceleration phenomenon of particles comparable to the throat size, discovered in the numerical study, will be experimentally verified in the future. The motion of two particles following different paths suggests that the converging-diverging microchannel can be utilized for passive separation and ordering of microparticles. Particles off the centerline of the converging-diverging microchannel rotate as they translate.

The NS-ALE finite-element model provides insights into certain experimental observations. Furthermore, the model can be used to test rapidly and inexpensively other biomicrofluidic applications, such as particle focusing,[37] ordering,[37] and separation.[38,39] With the coupling of particle structural analysis to the current NS-ALE model, it is also feasible to predict the pressure-driven transport of deformable particles in more realistic biomicrofluidic applications such as red blood cell separation,[40] deformation,[41,42] and DNA stretching[24] in biomicrofluidic devices.

ACKNOWLEDGMENTS

This work was supported, in part, by the Office of Research's Multidisciplinary Grant (S.Q.) and the Korea Research Foundation Grant No. KRF-2008-313-D00117 funded by the Korean Government (S.W.J.).

[1] T. M. Squires and S. R. Quake, Rev. Mod. Phys. **77**, 977 (2005).
[2] P. S. Dittrich and A. Manz, Nat. Rev. Drug Discovery **5**, 210 (2006).
[3] D. B. Weibel and G. M. Whitesides, Curr. Opin. Chem. Biol. **10**, 584 (2006).
[4] F. A. Gomez, *Biological Applications of Microfluidics* (Wiley Interscience, New Jersey, 2008).
[5] R. Johann and P. Renaud, Electrophoresis **25**, 3720 (2004).
[6] Z. Palkova, L. Vachova, M. Valer, and T. Preckel, Cytometry, Part A **59A**, 246 (2004).
[7] D. Stein, F. H. J. van der Heyden, W. J. A. Koopmans, and C. Dekker, Proc. Natl. Acad. Sci. U.S.A. **103**, 15853 (2006).
[8] J. W. Munyan, H. V. Fuentes, M. Draper, R. T. Kelly, and A. T. Woolley, Lab Chip **3**, 217 (2003).
[9] J. W. Kan, Z. G. Yang, T. J. Peng, G. M. Cheng, and B. Wu, Sens. Actuator, A **121**, 156 (2005).
[10] J. Happel and B. J. Byrne, J. Ind. Eng. Chem. (Seoul, Repub. Korea) **46**, 1181 (1954).
[11] W. L. Haberman, R. M. Sayre, and W. David, Taylor Basin Report No. 1143, 1958.
[12] R. G. Cox and S. G. Mason, Annu. Rev. Fluid Mech. **3**, 291 (1971).
[13] P. M. Bungay and H. Brenner, Int. J. Multiphase Flow **1**, 25 (1973).
[14] M. Iwaoka and T. Ishii, J. Chem. Eng. Jpn. **12**, 239 (1979).
[15] N. Al Quddus, W. A. Moussa, and S. Bhattacharjee, J. Colloid Interface Sci. **317**, 620 (2008).
[16] M. E. Staben and R. H. Davis, Int. J. Multiphase Flow **31**, 529 (2005).
[17] M. E. Staben, A. Z. Zinchenko, and R. H. Davis, J. Fluid Mech. **553**, 187 (2006).
[18] M. L. Plenert and J. B. Shear, Proc. Natl. Acad. Sci. U.S.A. **100**, 3853 (2003).
[19] X. C. Xuan, B. Xu, and D. Q. Li, Anal. Chem. **77**, 4323 (2005).
[20] S. Z. Qian, A. H. Wang, and J. K. Afonien, J. Colloid Interface Sci. **303**, 579 (2006).
[21] Y. J. Kang, D. Q. Li, S. A. Kalams, and J. E. Eid, Biomed. Microdevices **10**, 243 (2008).
[22] G. L. Lettieri, A. Dodge, G. Boer, N. F. de Rooij, and E. Verpoorte, Lab Chip **3**, 34 (2003).
[23] X. C. Xuan and D. Q. Li, J. Micromech. Microeng. **16**, 62 (2006).
[24] J. W. Larson, G. R. Yantz, Q. Zhong, R. Charnas, C. M. D'Antoni, M. V. Gallo, K. A. Gillis, L. A. Neely, K. M. Phillips, G. G. Wong, S. R. Gullans, and R. Gilmanshin, Lab Chip **6**, 1187 (2006).
[25] S. S. Hsieh and J. H. Liou, Biotechnol. Appl. Biochem. **52**, 29 (2009).
[26] D. W. Trahan and P. S. Doyle, Biomicrofluidics **3**, 012803 (2009).
[27] H. H. Hu, D. D. Joseph, and M. J. Crochet, Theor. Comput. Fluid Dyn. **3**, 285 (1992).
[28] H. H. Hu, N. A. Patankar, and M. Y. Zhu, J. Comput. Phys. **169**, 427 (2001).
[29] C. Z. Ye, D. Sinton, D. Erickson, and D. Q. Li, Langmuir **18**, 9095 (2002).
[30] C. Z. Ye and D. Q. Li, Microfluid. Nanofluid. **1**, 52 (2004).
[31] C. Z. Ye and D. Q. Li, J. Colloid Interface Sci. **272**, 480 (2004).
[32] C. Z. Ye, X. C. Xuan, and D. Q. Li, Microfluid. Nanofluid. **1**, 234 (2005).
[33] S. M. Davison and K. V. Sharp, Microfluid. Nanofluid. **4**, 409 (2008).

[34] S. M. Davison and K. V. Sharp, J. Colloid Interface Sci. **303**, 288 (2006).
[35] X. C. Xuan, C. Z. Ye, and D. Q. Li, J. Colloid Interface Sci. **289**, 286 (2005).
[36] Y. Ai, S. W. Joo, Y. Jiang, X. C. Xuan, and S. Qian, "Transient electrophoretic motion of a charged particle through a converging-diverging microchannel: Effect of direct current- dielectric force," Electrophoresis (in press).
[37] D. Di Carlo, D. Irimia, R. G. Tompkins, and M. Toner, Proc. Natl. Acad. Sci. U.S.A. **104**, 18892 (2007).
[38] D. Di Carlo, J. F. Edd, D. Irimia, R. G. Tompkins, and M. Toner, Anal. Chem. **80**, 2204 (2008).
[39] N. Pamme, Lab Chip **7**, 1644 (2007).
[40] S. Choi, S. Song, C. Choi, and J. K. Park, Lab Chip **7**, 1532 (2007).
[41] N. Korin, A. Bransky, and U. Dinnar, J. Biomech. **40**, 2088 (2007).
[42] N. Korin, A. Bransky, N. Lanir, Y. Nemirovski, and U. Dinnar, Biorheology **45**, 34 (2008).